Constitutive model of GH4720Li high temperature nickel base alloy at high strain rate and large temperature range

Jie Chen[a&b], Zhijun Wang[a,*], Haifeng Zhang[b], Hongtao Zhang[b], Qingxiang Yang[b], & Longhai Ye[b]

[a]School of Mechatronic Engineering North University of China, Taiyuan, 030 051, China

[b]Flight college, Anyang Institute of Technology, Anyang, 455 000, China

The dynamic mechanical properties of GH4720Li nickel base superalloy under high and low strain rates in a wide temperature range have been studied, and a constitutive model with higher fitting progress have been established. The experimental results show that the abnormal phenomenon of dynamic mechanical properties of GH4720Li alloy appears under the condition of high strain rate. This is because the change of Cr (MO) content in precipitates and the change of precipitate morphology lead to the difference of dynamic mechanical properties of GH4720Li alloy at high and low strain rates. Besides, A new piecewise function model based on a phenomenological representation of the stress-strain curves is proposed to describe the constitutive equation of Nickel-based superalloy GH4720Li of stress-strain curves. Meanwhile, new methods to obtain the material constant k and C are proposed to predicted accurately the flow stress. The comparison between calculated values and experimental values based on the new constitutive modeling shows that these methods for obtaining material constants k and C are valid and the new function model is significant for establishing constitutive equations of Nickel-based superalloy GH4720Li in hot deformation processes.

Keywords: Nickel-based superalloy, High strain rate, Low strain rate, Precipitate, Constitutive equation

1 Introduction

GH4720Li is an advanced high strength nickel base alloy, which has excellent high temperature mechanical properties and corrosion resistance. It is often used to manufacture rotating parts of aero turbine engines[1-5]. Therefore, the mechanical properties of GH4720Li alloy have always been one of the hot spots of many scholars. Wan[2] *et al.* investigated the high-temperature deformation behavior of an U720ULi alloy by the hot compression test at temperature of 1060-1080℃, strain rates of 0.001-10s[-1]. It demonstrated that the high activation energy for $\gamma + \gamma'$ dual-phase microstructures was mainly attributed to the precipitation hardening effect of $\gamma'(Ni_3(Al,Ti))$ particles. Zhao[3] *et al.* studied fine grain ingot casting technology of a Ni-base superalloy 720Li by the hot compression test at temperature of 1110-1150℃, strain rates of 0.001-0.1s[-1], and they found that a hot die forged pancake was produced with an ASTM 7 fine grain structure, which demonstrated the potential of GH720Li alloy disk to meet the component technical requirement. Liu[6] *et al.* studied the hot deformation behavior of U720Li alloy with fine, coarse and mixed grain by the hot compression test at temperature of 1040-1190℃, strain

rates of 0.01-0.5s[-1]. Base on the experimental results, in single-phase region, dynamic recrystallization (DRX) mainly occurred along the boundaries, while a decrease in the grain size accelerated the DRX kinetics. In two-phase region, the DRX on grain boundaries of coarse grain was limited. Yu[7] *et al.* identified a relationship between the dynamic recrystallization (DRX) and the presence of γ' precipitates for Udimet720Li by the hot compression test at temperature of 1070-1190℃, strain rates of 0.01-0.5s[-1]. For the coarse grain, the nucleation of DRX grains was influenced by the γ' interparticle spacing. Qu[8] *et al.* establish the constitutive equation and the processing map of GH4720Li alloy based on the flow stress during hot compression test at temperature of 1100-1170℃, strain rates of 0.01-1/s. Xie[9] *et al.* carried out uniaxial compression tests with strain rate of 0.01s[-1] on GH4720Li alloy at sub-solvus temperature (1110℃) and super-solvus temperature (1140℃). They used several different strains to characterize the deformation process and microstructure evolution process of the test pieces. The results revealed that the volume fraction of DRX grains increased with strain at both sub-solvus and super-solvus temperatures, and also the fraction of high angle grain boundaries. Besides, they also found that discontinuous dynamic recrystallization (DDRX)

was the main thermal deformation process of the test pieces at sub-solvus temperature and super-solvus temperature. Continuous dynamic recrystallization (CDRX) is the second mechanism inferior to discontinuous dynamic recrystallization. Continuous dynamic recrystallization played a very important role in the process of sub-solvus temperature plastic deformation, which was different from the reported dynamic recrystallization mechanism of billet fine grain structure. Their research results improved the understanding of DDRX and CDRX, helped to accurately control the microstructure of nickel base superalloys, and improved the performance of aeroengine components.

In conclusion, the research on dynamic mechanical properties of GH4720Li alloy was mainly focused on the condition of high temperature and low strain rate. However, there are few studies on the dynamic mechanical properties of GH4720Li alloy at medium low temperature and high strain rate.

Generally speaking, there is a large temperature difference in the rotating parts of aero-engine. For example, the volume of turbine blade is small and it is in a relatively narrow high temperature environment. However, aeroengine turbine disk is different. The volume of turbine disk is large, and there is a large temperature gradient in the working environment. For example, the inner diameter temperature of the turbine disk is the lowest, the edge temperature is the highest, and the web temperature is between the two. Therefore, it is of great practical significance to study the dynamic mechanical properties of GH4720Li alloy at medium and low temperature. Besides, the turbine discs suffer the scour by high-temperature and high-pressure gas and may be impact by foreign object, in other words, the turbine discs get damaged not only by creep and fatigue, but also impact, which may lead to the failure of engine[10]. Thus, it is very important to study the mechanical properties of GH4720Li alloy at high strain rate.

Generally, the mechanical properties of materials rely on the microstructure which, in turn, are controlled by hot deformation parameters such as temperature, strain and strain rate. Thus, the Constitutive equation with good fitting accuracy plays important roles in characterization of flow stress behavior, optimization of process parameters and microstructure control for metals and alloys during hot deformation. Consequently, it is of great value to study the dynamic mechanical properties of

GH4720Li alloy at high strain rate in a large temperature range and the relationship between its constitutive equation and strain rate and temperature.

In summary, the dynamic mechanical behavior of GH4720Li alloy at high strain rate in a large temperature range was studied, and the constitutive equation of the alloy was established in the form of piecewise function. The reason of abnormal dynamic mechanical properties of GH4720Li alloy at high strain rate was analyzed from the perspective of microstructure.

2 Materials and Methods

The chemical compositions of GH4720Li superalloys were measured as: C, Cr, Co, Al, Mo, B, Ti, Mn, Si, Nb, Ni and Fe. The size of specimen at strain rate of $10s^{-1}$ was $\emptyset$ 6mm × 9mm and the size of specimen at strain rate of $1000s^{-1}$ and $5000s^{-1}$ are $\emptyset$ 5mm × 5mm. Hot compression tests were conducted at temperature of 20℃, 200℃, 400℃, 800℃, 1000℃ and the strain rates were set to be $10s^{-1}$, $1000s^{-1}$ and $5000s^{-1}$, respectively. Uniaxial compression tests of the Nickel-base superalloy GH4720Li were conducted, and three duplicate tests were carried out each temperature and strain rate. To reduce the end friction during the compression tests, the specimen ends were first polished using waterproof silicon carbide paper and then greased in the tests. Prior to the hot compression, the specimens were heated to the deformation temperature at a rate 10℃/s and hold for 5 min to eliminate the thermal gradients as well as to ensure the uniform temperature of the specimens. Then, the specimen was compressed with a specified strain rate and quenched in water immediately to retain the microstructures at elevated temperature. Final, the specimens were after polished and etched in the corrosive solution. The change rules of the microstructure were observed by Scanning Electron Microscope (SEM). Energy Dispersive Spectrometry (EDS) attached to the SEM was utilized to examine the chemical composition of the phases formed in the samples. X-ray diffractometer (XRD) was used to determine the phase in the samples.

3 Results and Discussion

3.1 The true stress-strain curves

The true stress-strain cures of hot compression of GH4720Li superalloys under different conditions were shown in Fig. 1. It could be seen from Fig. 1(a) that the flow stress decreases gradually as the temperature
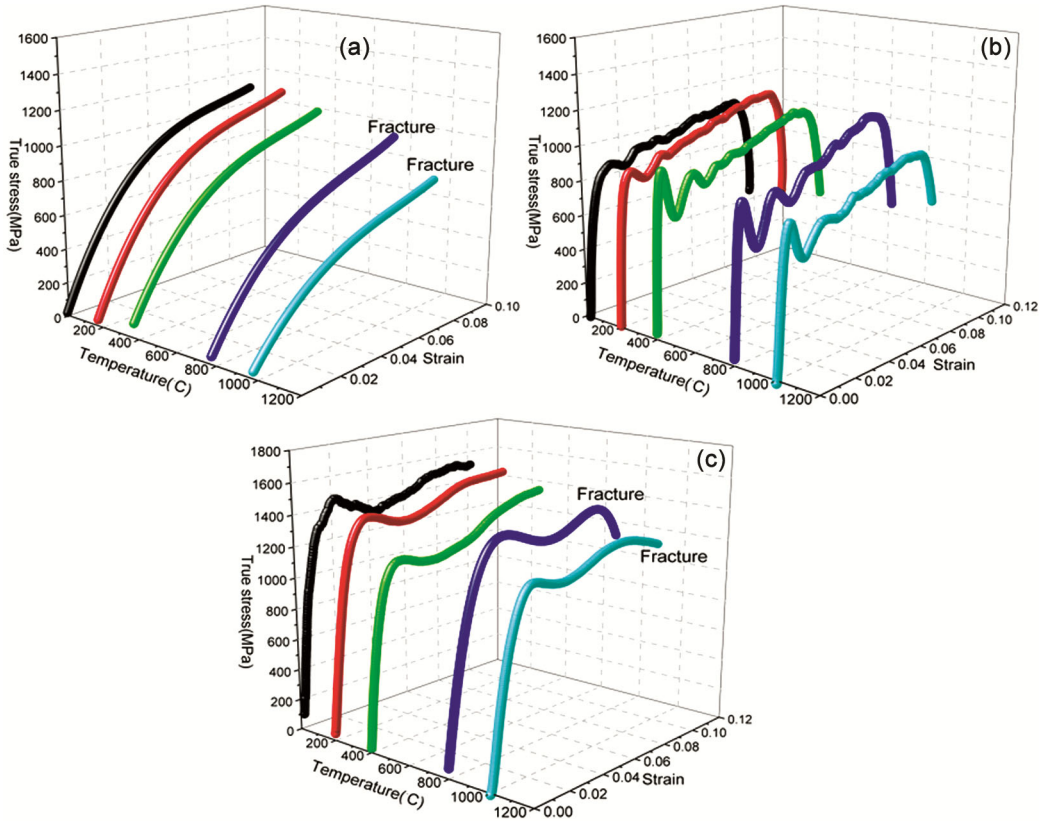
Fig. 1 — The true stress-strain curve of GH4720Li under the different conditions (a) 10s[-1], (b) 1000s[-1], and (c) 5000s[-1].

increases at the low strain rate (10s[-1]). However, the abnormal mechanical properties of GH4720Li Ni base superalloy appears at high strain rate (1000s[-1]/5000s[-1]). When the strain rate is 1000s[-1]/5000s[-1], the flow stress do not decrease with increase of deformation temperatures, on the contrary, when the temperature reaches 200℃, the true stress value of GH4720Li reached the maximum, followed by the stress value at 800℃. Under the condition of high strain rate, the stress values of GH4720Li from large to small were 200℃, 800℃, 400℃, 20℃, 1000℃, as shown in Fig. 1(b and c). Therefore, GH4720Li exhibits completely different mechanical properties at high and low strain rates. To further understand the anomalous phenomenon about flow stress of Nickel-based superalloy GH4720Li at high strain rates (1000s[-1]and 5000s[-1]), the flow stress-deformation temperature relationship was plotted in Fig. 2.

Figure 2 shows the flow stress vs deformation temperature with various strain rates and strains. Generally, plastic deformation produces a lot of heat. For the loading at high strain rate, there is no sufficient time for this heat to dissipate into the surroundings. The actual temperature in consideration of significant increased in temperature with a specimen can be estimated by[11,12]:

$$T = T_0 + \Delta T = T_0 + \int_0^{\varepsilon} \frac{\eta}{\rho c_{\mathrm{v}}} \sigma \mathrm{d}\varepsilon \qquad \dots (1)$$

where, T_0 is the initial temperature in compressive experiments, ΔT is the increasement in temperature within specimen caused by the adiabatic process under high-rate loading, C_{v} is the heat capacity, ρ is the density of the material, ε is the plastic strain, σ is the flow stress and η is the fraction of the heat generated by the plastic work that applies to the sample.

As seen in Fig. 2 (a-c), for the studied range of temperatures (20℃~1000℃) and the selected strain rates (10, 1000 and 5000/s), When the strain rate was 10s[-1], the true stress decreases with the increase of temperature; When the strain rate increases to 1000s[-1] / 5000s[-1], the real stress increases with the increase of temperature (20℃~200℃); when the temperature continue to increase to 400℃, the stress decreased gradually, when the temperature reaches 800℃, the stress begin to increase with the increase of temperature, when the temperature increases to 1000℃, the stress begin to weaken.
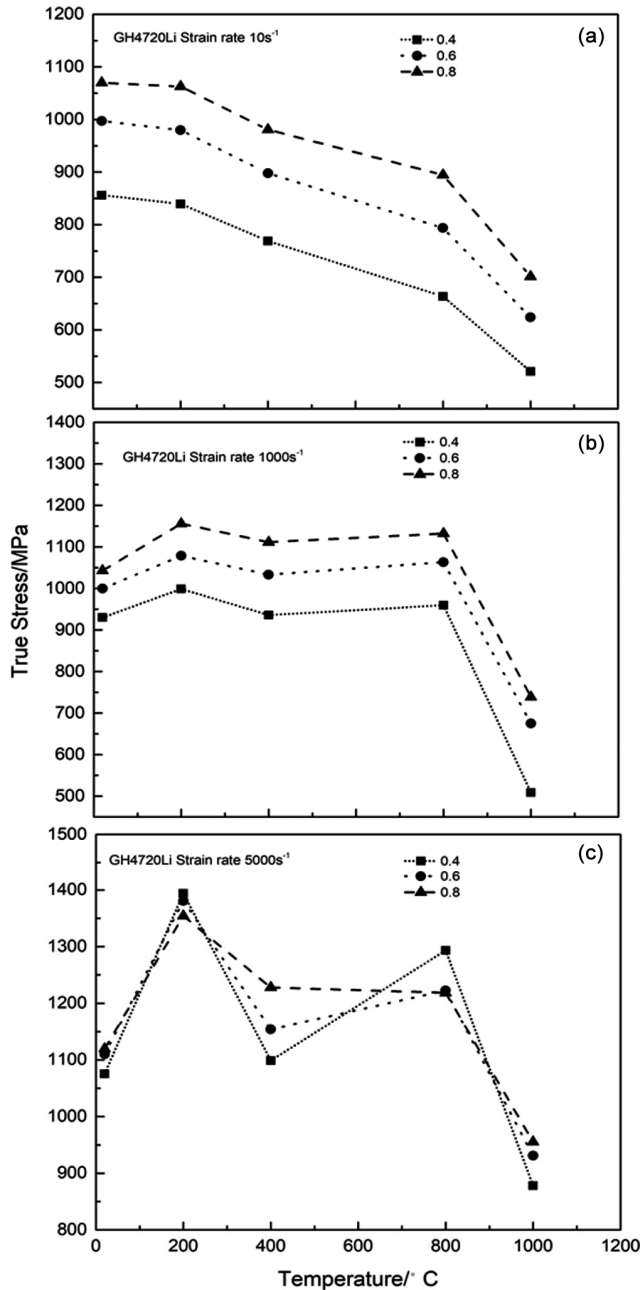
Fig. 2 — The flow stress vs temperature relations with strain rate of (a) 10/s, (b) 1000/s, and (c) 5000/s.

3.2 Microstructures of deformed specimens

Figure 3 was EDS energy spectrum of the original test piece of GH4720Li alloy. It can be seen from Fig. 3 that Cr (Mo) and Fe was relatively abundant in GH4720Li alloy.

Figure 4 shown the microstructure of the Nickel-based superalloy GH4720Li under different conditions.

Figure 5 presented the XRD patterns of the GH4720Li under different test conditions.

Figure 4 (a) shows the initial microstructure of GH4720Li specimen before compression test. Figure 5 (a) shown the XRD pattern of GH4720Li specimen before compression test. As shown in Fig. 5 (a), GH4720Li specimen did not have any precipitates before compression test. However, it can be seen from Fig. 4 (b and c) and Fig. 5 (b and c) that a large number of white precipitates appears after the low strain rate ($10s^{-1}$) compression test. The comparison between Fig. 4 (b and c) show that the morphology of the two precipitates is different. The white precipitates in Fig. 4 (b) are needle like, but their true shape is lamellar[2]. Then, the white precipitates in Fig. 4 (c) are spherical[13,14]. The appearance of these two white precipitates is related to Mo[14]. EDS analysis shown that the white precipitate contains a lot of Cr and Mo elements, as show in Fig. 6 (a and b). Under the condition of low strain rate ($10s^{-1}$), the true stress of GH4720Li decreases with the increase of temperature, which is related to the white precipitate containing Cr (Mo). That was to say, the precipitates containing Cr (Mo) let to the decrease of compressive strength. This was consistent with the previous investigation that the Cr(Mo) phase results in the deterioration of the properties of Ni-base alloys[15,16]. Base on the compressive strength of Cr(Mo) lamellar phase is higher than that of Cr(Mo) spherical phase[2], therefore, in the case of low strain rate ($10s^{-1}$), the true stress value of GH4720Li at 800 ℃ is smaller than that at 20 ℃. When the strain rate is increased to $1000/5000s^{-1}$, the precipitates appeared in the specimen at the same temperature, as show in Fig. 4 (d-g), which is different from that in the low strain rate ($10s^{-1}$) experiment, as shown in Fig. 5 (a-g). It can be seen from Fig. 6 (c-f) that when the strain rate is $1000/5000s^{-1}$, the precipitate contains a large amount of Fe, and its Cr content decreases significantly. Through the comparison between Fig. 6 (a and b) and Fig. (c-f), it can be found that the content of Fe is higher than before, and the content of Cr is greatly reduced. Moreover, the content of Ni also decreases. This shows that Fe occupies Ni site. Previous investigation reported that Fe has a strengthening effect on Ni-base alloy when Fe mainly occupies the Ni site[2]. Thus, at the same temperature, the true stress of GH4720Li at high strain rate was larger than that at low strain rate. Furthermore, the increase of Fe content resulted in the increasement of metallic bond and the decreasement of covalent bond,
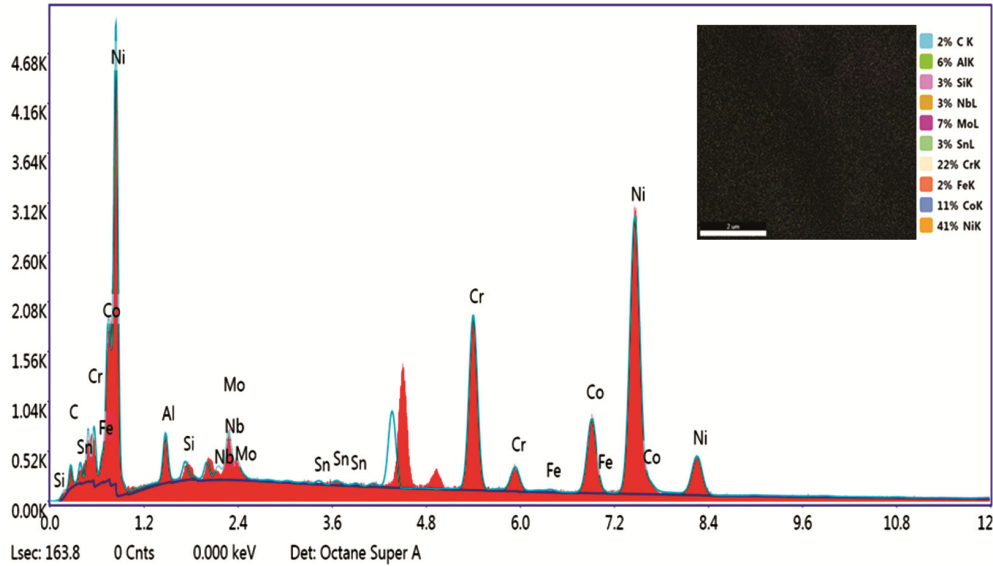
Fig. 3 — EDS energy spectrum of the original test piece of GH4720Li alloy.

as reported by Kovalev *et al.*[2]. Generally, the increasement of metallic bond could improve the ductility for mental materials, as shown in Fig. 1(c). Therefore, when GH4720Li was at high strain rate(1000/5000s⁻¹), especially when the strain rate is 5000s⁻¹, both the strength and the ductility increase. At the strain rate of 1000s⁻¹, the XRD patterns of the precipitates at 20 °C and 800 °C were similar, as shown in Fig. 5 (e and f), and there were a lot of Fe elements in the precipitates of both, and the difference of Fe content is not obvious as shown in Fig. 6 (c and d). Therefore, under the condition of strain rate of 1000s⁻¹, the true stress value of GH4720Li at 20 °C and 800 °C had little difference, as shown in Fig. 2 (b). When the strain rate is 5000s⁻¹, the Fe content in the precipitate at 20 °C is less than that in the precipitate at 800 °C, as shown in Fig. 6 (e and (f). Therefore, the true stress value of GH4720Li at 800 °C is larger than that at 20 °C.

In conclusion, the difference of mechanical properties of GH4720Li Ni base superalloy at high and low strain rates, or the abnormal mechanical properties of GH4720Li at high strain rate are caused by the different morphology of precipitates and the different contents of Fe, Cr (Mo) in the precipitates.

3.3 The establishment of constitutive modeling

3.3.1 Determination of peak stress

A typical kinetic relationship between the strain rate, deformation temperature and flow stress at high deformation temperature is typically expressed by the Arrhenius equation as:

$$\dot{\varepsilon} = A[\sinh{(\alpha\sigma)}]^n \exp{(-Q/RT)} \qquad \ldots (2)$$

where A, α and n are constants, $\dot{\varepsilon}$ is the strain rate, Q is the deformation activation energy, R is the universal gas constant, T is the deformation temperature. The effects of temperature and strain rate on the peak flow stress can be expressed by the Zener-Holloman parameter Z in an exponential form. The hyperbolic law in an Arrhenius type equation gives better approximation between Zener-Hollomon parameter and flow stress:

$$Z = A[\sinh{(\alpha\sigma)}]^n = \dot{\varepsilon}\exp\left(-\frac{Q}{RT}\right) \qquad \ldots (3)$$

The flow stress can be considered as a function of Zener-Hollomon parameters,

$$\sigma = \frac{1}{\alpha}\ln\left\{\left(\frac{Z}{A}\right)^{\frac{1}{n}} + \left[\left(\frac{Z}{A}\right)^{\frac{2}{n}} + 1\right]^{0.5}\right\} \qquad \ldots (4)$$

In order to determine the peak flow stress at evaluated temperatures and strain rates, a relationship between the peak flow stress and Zener-Hollomon parameter Z is written as the power law of Eq. (5) at low stress level, and as the exponential law of Eq. (6) at high stress level:

$$\dot{\varepsilon} = A_1\sigma^{n_1}\exp{(-Q/RT)} \qquad \ldots (5)$$

$$\dot{\varepsilon} = A_2\exp{(\beta\sigma)}\exp{(-Q/RT)} \qquad \ldots (6)$$

where, A_1, A_2, β and n_1 are the materials constant.

Taking the natural logarithm on both sides of Eq. (5) and (6), respectively:

$$ln\dot{\varepsilon} = lnA_1 - \frac{Q}{RT} + n_1 ln\sigma \qquad \text{... (7)}$$

$$ln\dot{\varepsilon} = lnA_2 - \frac{Q}{RT} + \beta\sigma \qquad \text{... (8)}$$

So, the values of n_1 and β can be calculated by the following equation by differentiating Eqs (7) and (8), respectively.

$$n_1 = [\frac{\partial ln\dot{\varepsilon}}{\partial ln\sigma}]_T \qquad \text{... (9)}$$

$$\beta = [\frac{\partial ln\dot{\varepsilon}}{\partial \sigma}]_T \qquad \text{... (10)}$$

Then, the peak flow stresses at different temperatures and strain rates measured from the flow stress-strain curves were selected to describe the relationship of $ln\dot{\varepsilon}$-$ln\sigma$ and $ln\dot{\varepsilon}$-σ, as shown in Fig. 7(a and b). It can be observed that the flow stresses are well fitted by a group of straight lines. Therefore, n_1 and β can be calculated from the slopes of the line, where n_1=13.8195Mpa^{-1} and β=0.01162. Thus, the material parameter of $\alpha = \frac{\beta}{n_1} = 0.0008$.

Taking the natural logarithm of Eq. (2), the constant of Q can be expressed as:

$$Q = R\{\frac{\partial ln\dot{\varepsilon}}{\partial \ln[\sinh(\sigma\alpha)]}\}_T\{\frac{\partial \ln[\sinh(\sigma\alpha)]}{\partial(1/T)}\}_{\dot{\varepsilon}} \qquad \text{... (11)}$$
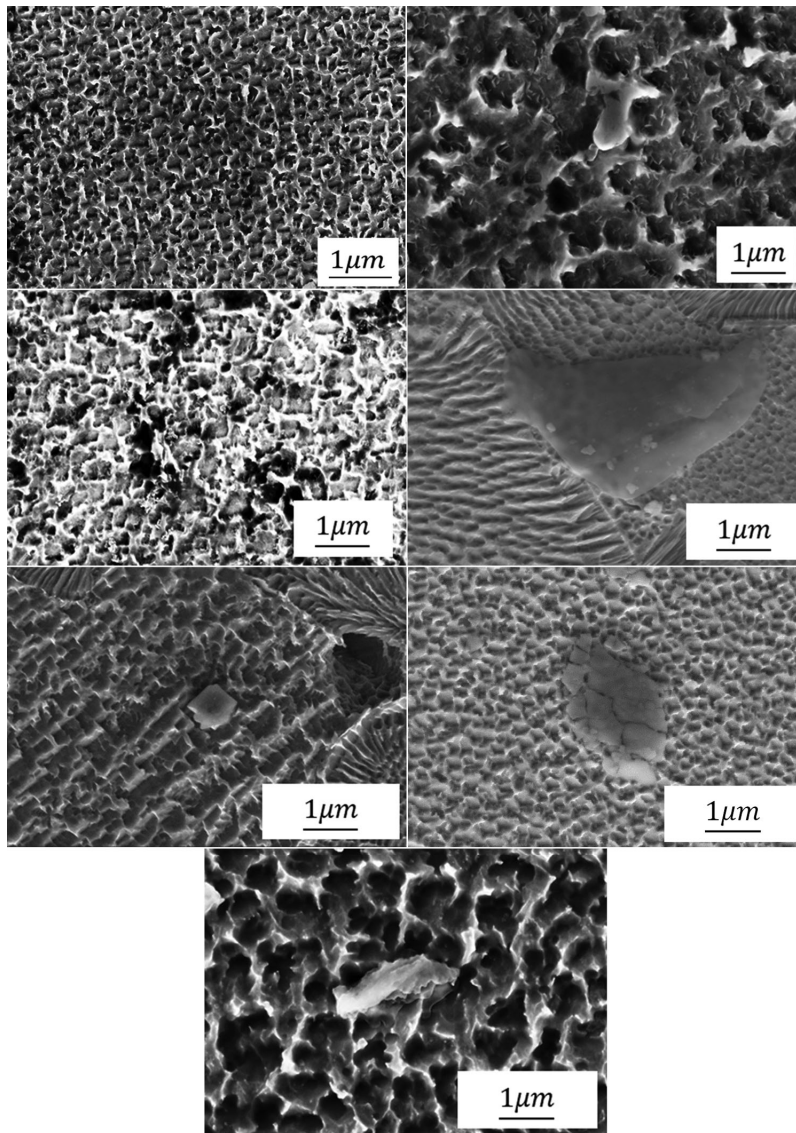

Fig. 4 — The microstructure of the Nickel-based superalloy GH4720Li under different conditions: (a) initial microstructure, (b)10s^{-1}, 20°C, (c) 10s^{-1}, 800°C, (d)1000s^{-1}, 20°C, (e)1000s^{-1}, 800°C, (f) 5000s^{-1}, 20°C, and (g) 5000s^{-1}, 800°C
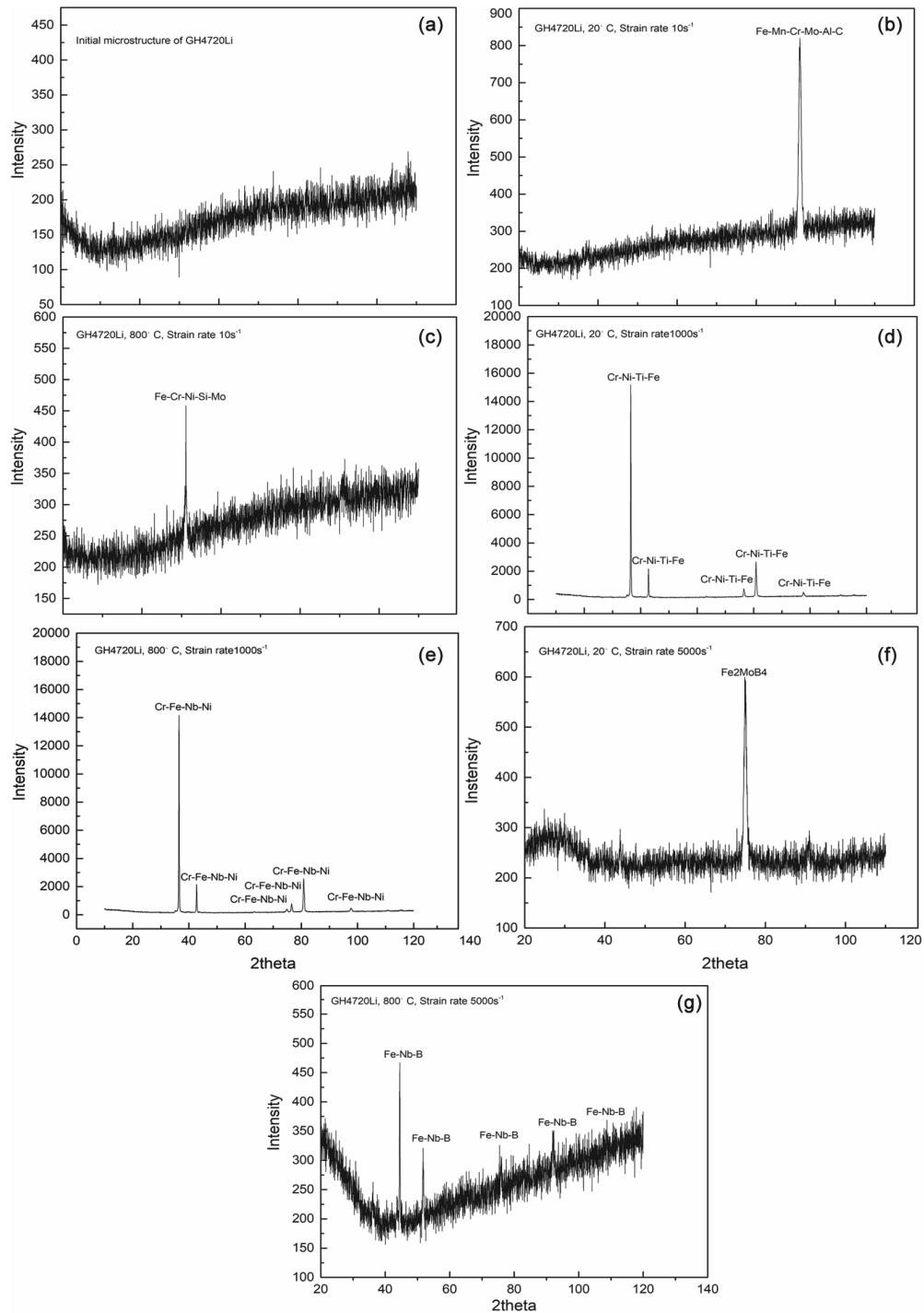
Fig. 5 — The XRD patterns of the GH4720Li under different test conditions: (a) initial microstructure; (b)10s^{-1}, 20℃,(c)10s^{-1}, 800℃, (d) 1000s^{-1},20℃ (e) 1000s^{-1}, 800℃, (f) 5000s^{-1}, 20℃, and, (g) 5000s^{-1}, 800℃.

Similarly, the peak flow stress and its corresponding temperature and strain rate were used to describe the relationship of $ln\dot{\varepsilon}$-ln[sinh($\sigma\alpha$)] and $1/T$ -ln[sinh($\sigma\alpha$)] as shown in Fig. 7(c and d). The values can be determined by calculating the average slopes of fitting lines in Fig. 7(c and d).

The values of material constants of n and A can be obtained by taking the natural logarithm on both sides of Eq. (3):

$$lnZ = lnA + n\ln[\sinh(\sigma\alpha)] \qquad\qquad \dots (12)$$

Figure 8 shown the relationship between *lnZ* and ln[sinh($\sigma\alpha$)]. Thus, the slop and intercept of straight line in Fig. 8 are used to evaluate the values of *n* and *lnA*. In this study, the calculated values of n and A are 8.76347 and 518.1942.

The deformation activation energy is significantly affected by the deformation temperature and strain rate, as shown in Fig. 9. However, the influence of the deformation temperature and strain rate on the flow stress is not considered in the above Arrhenius type model in Eq. (4). Hence, it was imperative to take into account the influence of the deformation temperature and strain rate on the flow stress in constitutive model to describe the flow stress more accurately. A second order polynomial fitting can be applied to well describe the relationship between the deformation temperature and strain rate and deformation activation energy *Q*, as expresses in the following equation:

$$Q = A_0 + A_1T + A_2\dot{\varepsilon} + A_3T^2 + A_4\dot{\varepsilon}^2 + A_5T\dot{\varepsilon} \quad \dots (13)$$

The polynomial fitting results are listed in Table 1. The peak stress under different conditions can be calculated by means of these material constants and the above equations. The predicted values was in good agreement with the experimental data, as shown in Fig. 10, and the Arrhenius equations established are reliable for describing the peak stress and are suitable for numerical simulations of rigid plastic deformation.
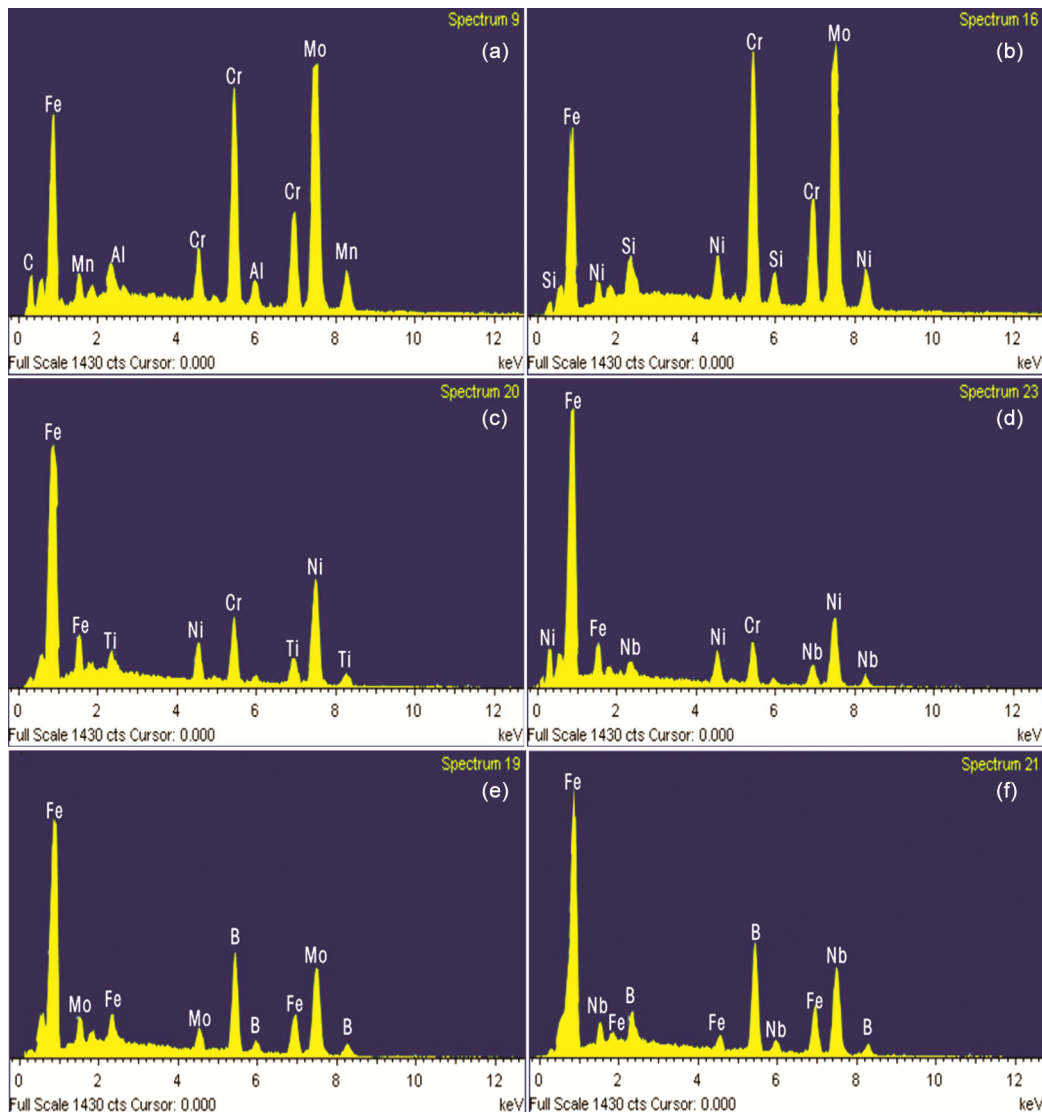

Fig. 6 — The EDS spectra of GH4720Li under different deformation conditions: (a)10s^{-1}, 20℃, (b) 10s^{-1}, 800℃, (c)1000s^{-1}, 20℃, (d)1000s^{-1}, 800℃, (e) 5000s^{-1}, 20℃, and (f) 5000s^{-1}, 800℃.
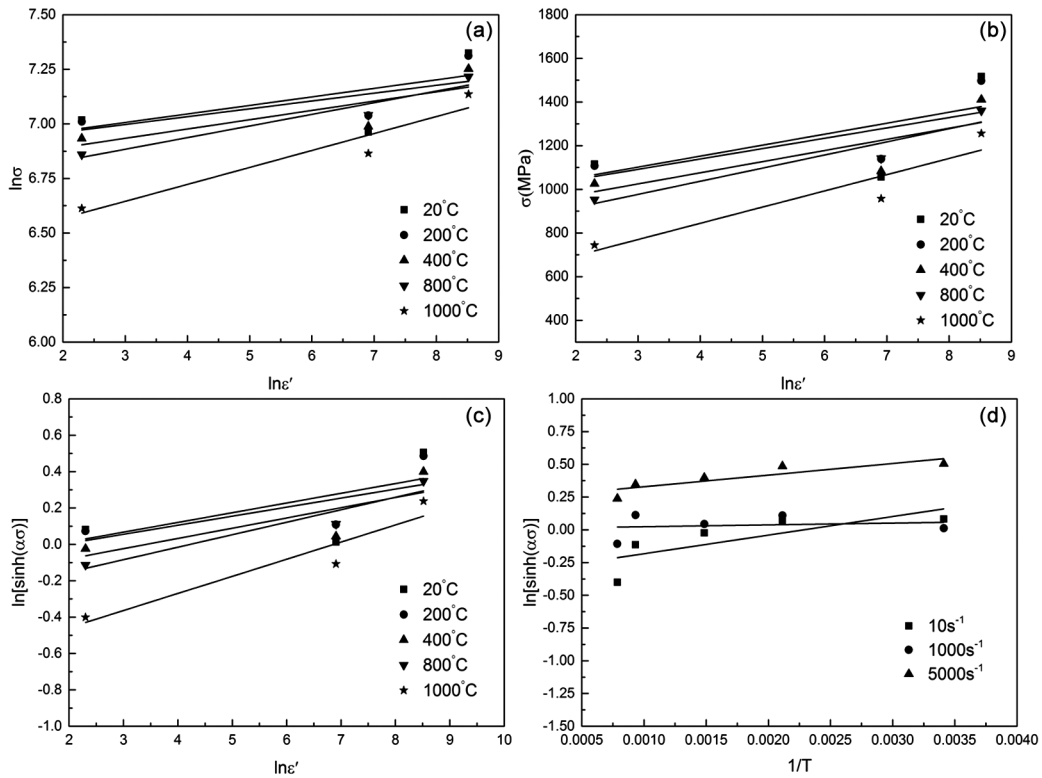
Fig. 7 — Relationship between: (a) $ln\dot{\varepsilon}$- $ln\sigma$, (b) $ln\dot{\varepsilon}$-σ, (c) $ln\dot{\varepsilon}$-ln[sinh($\sigma\alpha$)], and (d) $1/T$ - ln[sinh($\sigma\alpha$)].
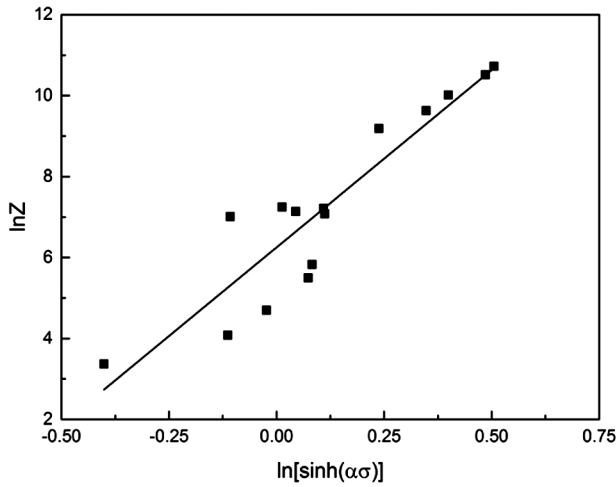

Fig. 8 — Relationship between ln[sinh($\sigma\alpha$)]- lnZ.

Fig. 9 — Relationship between Q and temperature and $ln\dot{\varepsilon}$.

3.3.2 Piecewise function models

A high efficient constitutive equation with the better precision and more wide range of strain had more significant help to optimize the processing parameters and employ mathematical simulations in metal forming. In order to predict the experimental data of the materials more accurately, a new piecewise function models are proposed to describe the constitutive equations.
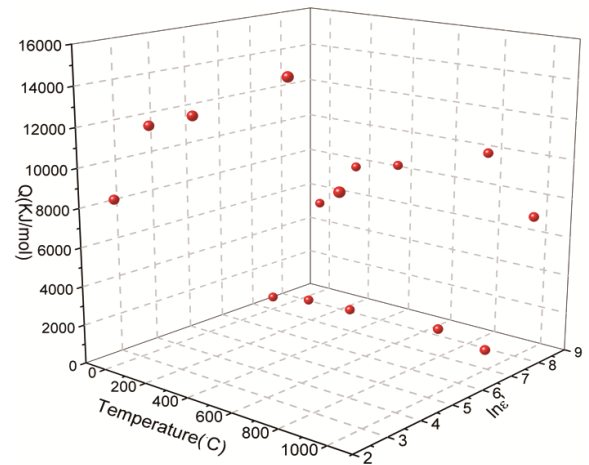
3.3.2.1 Modeling of flow stress in the first stage($\varepsilon \leq 0.03$)

According to previous studied, the stress-strain curves with the range of strain from initial to the strain 0.03 can be described using the following equation[17-20]:

$$\frac{\sigma}{\sigma_{0.03}} = [(\frac{\varepsilon}{\varepsilon_{0.03}})\exp{(1 - \frac{\varepsilon}{\varepsilon_{0.03}})}]^{C} \qquad \qquad \dots (14)$$

where, $\sigma_{0.03}$ was the stress at strain 0.03. Taking the natural logarithm of both sides of Eq. (14), and the following equation is obtained:

Table 1 — Coefficients of polynomial function of material parameters

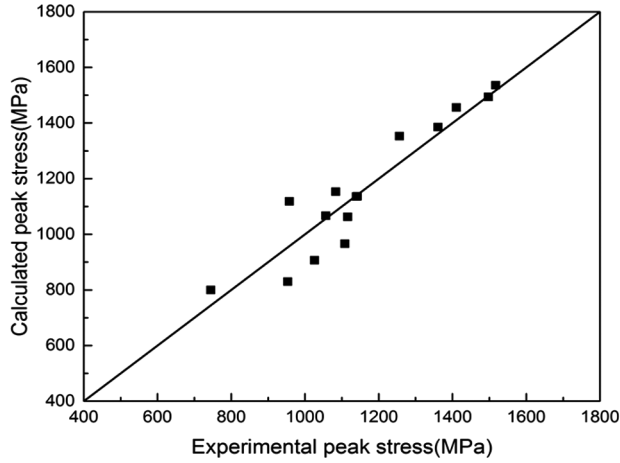| A	B	C	D
$A_0=5.132\times10^3$	$B_0=-8.900\times10^{-3}$	$C_0=1.971\times10^4$	$D_0=1.023$
$A_1=20.87$	$B_1=-3.940\times10^{-3}$	$C_1=-2.315\times10^5$	$D_1=2.420\times10^{-4}$
$A_2=-13.84$	$B_2=-3.306\times10^{-2}$	$C_2=1.323\times10^6$	$D_2=-2.512\times10^{-2}$
$A_3=-1.200\times10^{-2}$	$B_3=1.349\times10^{-6}$	$C_3=5.186\times10^6$	$D_3=-5.6848\times10^{-7}$
$A_4=2.590\times10^{-2}$	$B_4=1.396\times10^{-2}$		$D_4=-7.510\times10^{-3}$
$A_5=-4.966\times10^{-5}$	$B_5=3.684\times10^{-4}$		$D_5=6.028\times10^{-5}$

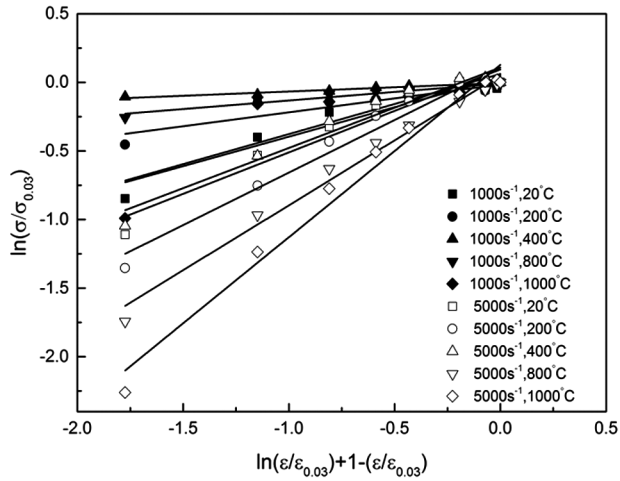Fig. 10 — Relationship between experimental peak stress and calculated peak stress.

Fig. 12 — Variations of k with strain rate and deformation temperature and strain.

$$C = B_0 + B_1T + B_2ln\dot{\varepsilon} + B_3T^2 + B_4(ln\dot{\varepsilon})^2 + B_5Tln\dot{\varepsilon} \quad\text{… (16)}$$

The polynomial fitting results are listed in Table 1.

3.3.2.2 Modeling of flow stress in the second stage($\varepsilon \geq 0.03$)

The constitutive equation of flow stress with the range of strain from 0.03 to 0.1 can be written as the function[18,21,22]:

$$\sigma = \sigma_p - k(\varepsilon_p - \varepsilon) \quad\text{… (17)}$$

The values of k under different temperature, strain rate and strain are shown in Fig. 12. k can be described using the following equation:

$$k = (C_0 + C_1\varepsilon + C_2\varepsilon^2 + C_3\varepsilon^3)(D_0 + D_1T + D_2ln\dot{\varepsilon} + D_3T^2 + D_4(ln\dot{\varepsilon})^2 + D_5Tln\dot{\varepsilon}) \quad\text{… (18)}$$

The polynomial fitting results are listed in Table 1.

Thus, based on a phenomenological representation of the stress-strain curves, the constitutive modeling of GH4720Li considering the effect of strain, deformation temperatures and strain rates on flow stress can be established during high temperature deformation, the expression is as follow:

Fig. 11 — Relationship between $[ln\left(\frac{\varepsilon}{\varepsilon_{0.03}}\right) + (1 - \frac{\varepsilon}{\varepsilon_{0.03}})]$- $ln\left(\frac{\sigma}{\sigma_{0.03}}\right)$.

$$ln\left(\frac{\sigma}{\sigma_{0.03}}\right) = C[ln\left(\frac{\varepsilon}{\varepsilon_{0.03}}\right) + (1 - \frac{\varepsilon}{\varepsilon_{0.03}})] \quad\text{… (15)}$$

As shown in Fig. 11, the deformation temperature and strain rate are important for determining the material constant C and the tendency of C to change with temperature and strain rate is respectively linear. Therefore, the follow equation was proposed to describe the material constant C:
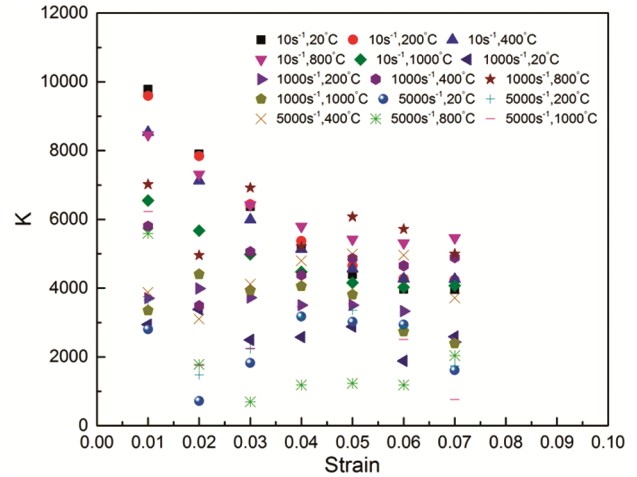
$$\begin{cases} \sigma = \sigma_{0.03}[(\sigma/\sigma_{0.03})\exp(1-\sigma/\sigma_{0.03})]^C (\varepsilon \le 0.03) \\ \sigma = \sigma_p - k(\varepsilon_p - \varepsilon)(\varepsilon \ge 0.03) \\ C = -8.900 \times 10^{-3} - 3.940 \times 10^{-3}T - 3.306 \times 10^{-2}ln\dot\varepsilon \\ \quad +1.349 \times 10^{-6}T^2 + 1.396 \times 10^{-2}(ln\dot\varepsilon)^2 \\ \quad +3.684 \times 10^{-4}Tln\dot\varepsilon \\ k = (1.97 \times 10^4 - 2.315 \times 10^5\varepsilon + 1.323 \times 10^6\varepsilon^2 + 5.186 \times 10^6\varepsilon^3) \\ \quad \times (1.023 + 2.420 \times 10^{-4}T - 2.512 \times 10^{-2}ln\dot\varepsilon - 5.6848 \times 10^{-7}T^2 - \\ \quad 7.510 \times 10^{-3}(ln\dot\varepsilon)^2 + 6.028 \times 10^{-5}Tln\dot\varepsilon) \\ \sigma_p = \frac{1}{0.0008}ln\left\{ \left(\frac{Z}{518.1942}\right)^{\frac{1}{8.76347}} + [(\frac{Z}{518.1942})^{\frac{2}{8.76347}} + 1]^{0.5} \right\} \\ Z = \dot\varepsilon\exp\left(-Q/RT\right) \\ Q = 5.132 \times 10^3 + 20.87T - 13.84\dot\varepsilon - 1.200 \times 10^{-2}T^2 + 2.590 \times 10^{-2}\varepsilon^2 - 4.966 \times 10^{-5}T\dot\varepsilon \end{cases}$$
$$\dots (19)$$

3.4 Validation and discussion of the constitutive modeling

Figure 13 shows a comparison between the flow stress calculated by the piecewise function model and our experiment data under different conditions. The flow stress obtained from the piecewise model is in good agreement with the experiment data, and the piecewise function methods for modeling the constitutive equation are effective and reliable.

Figure 14 depicts the correlation between experimental values and calculated values under different conditions. On the coordinate plane, if the calculated values were the same with the experimental values, the position of points would be near the line of Y=X. It was easy to find that the correlation coefficient (R) and the average absolute error (AARE) according to the result of analysis software are as follows[23]:
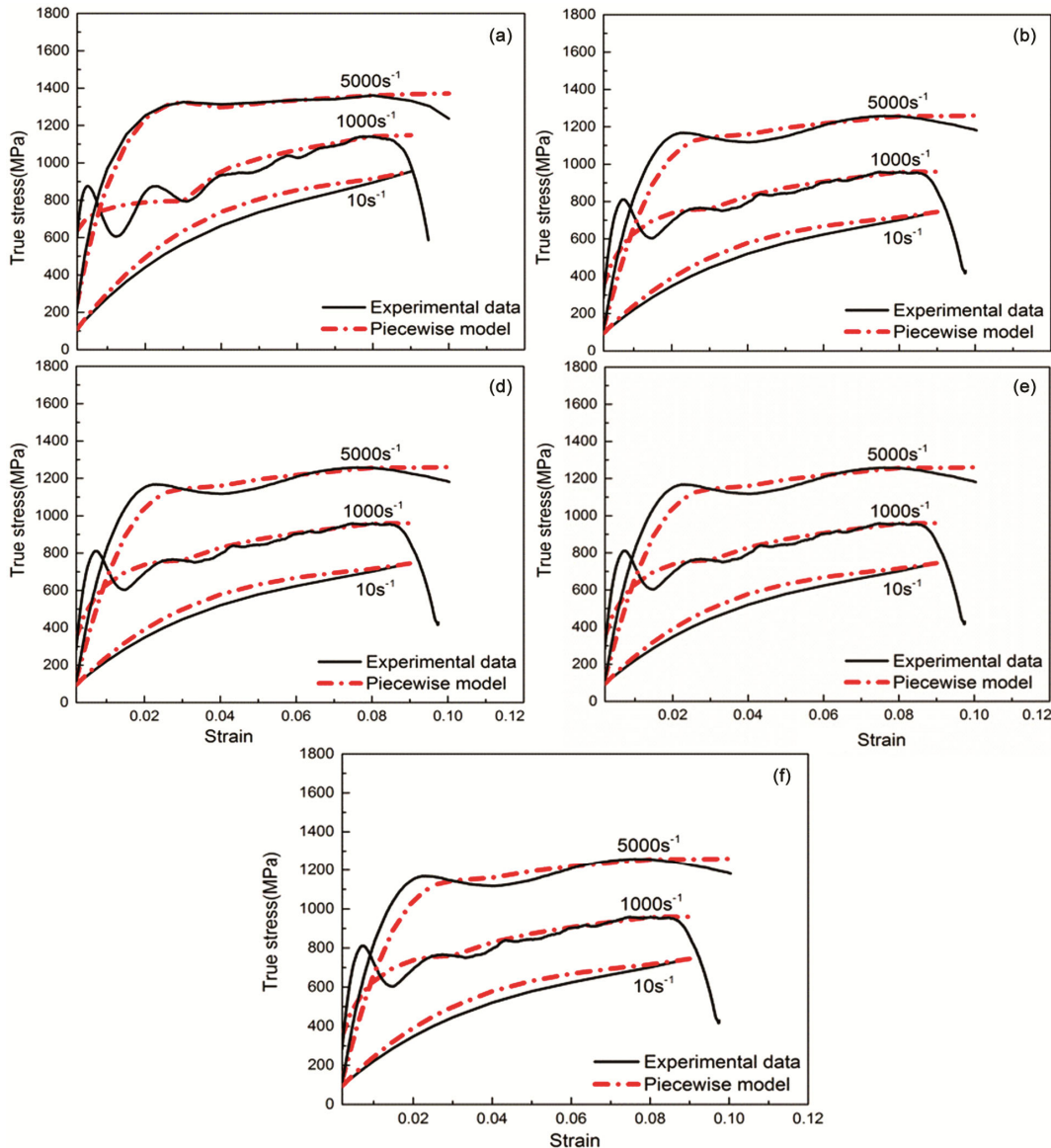

Fig. 13 — The comparison between values and calculated values at different deformation temperatures (a) 20℃, (b)200℃, (c)400℃, (d)800℃, and (e)1000℃.
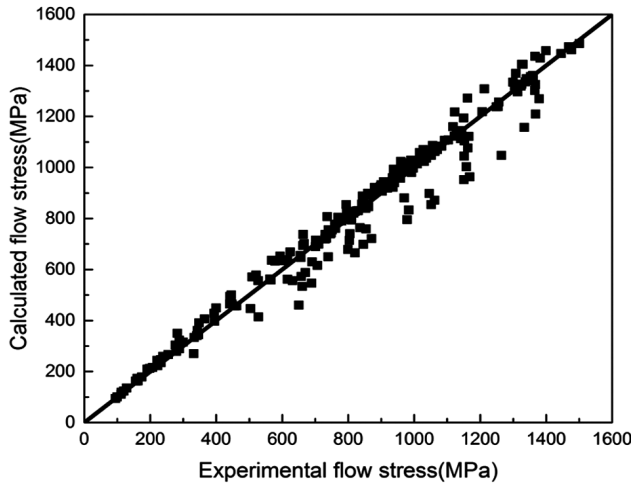
Fig. 14 — The correlation between experimental values and calculated values.

$$R = \frac{\sum_{i=1}^{N}(X_i-\bar{X})(Y_i-\bar{Y})}{\sqrt{\sum_{i=1}^{N}(X_i-\bar{X})^2}\sqrt{\sum_{i=1}^{N}(Y_i-\bar{Y})^2}} = 0.9987 \qquad \dots (20)$$

$$AARE(\%) = \frac{1}{N}\sum_{i=1}^{N}\left|\frac{X_i-Y_i}{X_i}\right| = 5.569\% \qquad \dots (21)$$

where, X_i is the experimental value of the stress from the hot compression test and Y_i is the calculated value of the stress from the constitutive modeling. $\bar{X}$ and $\bar{Y}$ are the mean values of X_i and Y_i respectively, and N is the total number of the data used in the equation. The correlation coefficient was between 0 and 1. The data fitted the regression line well if the correlation coefficient was near 1^{23}. The average absolute error (AARE) means the deviation between single value and the mean value, every single value was close to the mean value if the average absolute error (AARE) is near 0^{23}. Zhang *et al.* studied the hot compression deformation behavior of GH4698 alloy by Arrhenius constitutive modeling and the correlation coefficient and AARE are 0.955 and 3.98% respectively[21]. Wu *et al.* researched hot compression deformation behavior of a new Nickel-based superalloy base on Arrhenius constitutive modeling and the AARE is 3.81%[24]. Shamsolhodaei *et al.* studied the hot compression deformation behavior of Nickel-based superalloy using Arrhenius constitutive modeling and the correlation coefficient and AARE are 0.985 and 6.05% respectively[25]. However, Shamsolhodaei also developed the constitutive by using Zerilli-Armstrong equation, as a result, the correlation coefficient and AARE are 0.976 and 10.31% respectively.

In this paper, the hot deformation behavior of the Nickel-based superalloy GH4720Li was studied by using Arrhenius constitutive modeling, the correlation coefficient and the average absolute relative error between the predicted values and the measured values are 0.9987 and 5.569% respectively. This shows that the good correlation between experimental values and calculated values. All the discussion above shows that the constitutive modeling of GH4720Li established in this paper by using Arrhenius constitutive modeling is suitable, and the methods proposed to model material constants *k* and *C* are effective.

4 Conclusion

In this paper, the hot compression tests have been conducted over a wide range of temperature (20~1000℃) and strain rate(10~5000s^{-1}) to obtain further understandings of the deformation behavior of a Nickel-based superalloy GH4720Li. It is found that the mechanical properties of GH4720Li nickel base superalloy show different trends under high and low strain rates. The reasons for the difference are analyzed from the perspective of microstructure. The following conclusions are drawn:

I   The mechanical properties of GH4720Li Ni base alloy show different trends under high and low strain rates during compression deformation with a wide range of temperature changes. Under the condition of low strain rate (10s^{-1}), the true stress of GH4720Li decreases with the increase of temperature; however, under the condition of high strain rate (1000/5000s^{-1}), the mechanical properties of GH4720Li do not decrease with the increase of temperature, on the contrary, the abnormal phenomenon that the stress increases with the increase of temperature appears. This anomalous phenomenon is different from our common sense, which the flow stress decreases successively with increasing temperature.

II   The reason why the true stress of GH4720Li decreases with the increase of temperature is that the precipitate contains a lot of Cr (Mo). The precipitates containing Cr (Mo) lead to the decrease of plasticity and compressive strength of GH4720Li. The effect of Cr (Mo) precipitates with different morphologies on the compressive strength is different. The strength

of lamellar Cr (MO) precipitates is higher than that of spherical Cr (MO) precipitates. Therefore, in the case of low strain rate ($10s^{-1}$), the true stress value of GH4720Li at 800 ℃ is smaller than that at 20 ℃.

III   Under the condition of high strain rate ($1000/5000s^{-1}$), the content of Fe in GH4720Li precipitates increases, but the content of Cr (MO) decreases. With the increase of Fe content, more metal bonds are formed and the content of chemical bond is reduced, which improves the compressive strength and plastic properties of GH4720Li. Therefore, the mechanical properties of GH4720Li are abnormal at high strain rate.

IV   A new piecewise function model are proposed to describe the constitutive equation by the phenomenological representation of stress-strain curves. New methods are also developed to obtain the material constants k and C to improve prediction precision. The peak stress can be represented by the Zener-Hollomon parameter in a hyperbolic sine equation. Based on the new piecewise function model, the effects of the strain, strain rate and temperature on the flow stress is described.

V   The correlation coefficient and the average absolute relative error between the predicted values and the measured values are 0.9987 and 5.569% respectively. Besides, the comparison and discussion between experimental values under the condition of tests and calculated values based on the constitutive modeling shows that the constitutive equation modeling in the present work is valid and suitable, and the methods proposed to model material constants k and C are effective.

Acknowledgment

References

1   Hu D Y, Tian T, Wang X, Mao J X, Xiao Z X, & Wang R Q, *Int J Mech Sci,* 209 (2021) 106.

2   Wan Z P, Hu L X, Sun Y, Wang T, & Li Z, *J Alloys Compd*, 769 (2018) 367.

3   Chen J, Zhang H F, Zhang Y L, Zhang H T, Yang Q X, & Ye L H, *Int J Photoenergy*, 2021 (2021).

4   Hu D, Ma Q, Shang L, Gao Y, & Wang R *Mater Sci Eng*, 670 (2016A) 17.

5   Chang L T, Jin H, Sun W R, *J Alloys Compd*, 653 (2015) 266.

6   Liu F F, Chen J Y, Dong J X, Zhang M, & Yao Z, *Mater Sci Eng A*, 651 (2016) 102.

7   Yu Q Y, Yao Z H, Dong J X, *Mater Char*, 107 (2015) 398.

8   Qu J L, Bi Z N, Du J H, *et al.*, *J Iron Steel Res Int*, 18 (2011) 59.

9   Xie B C, Yu H, Tao S, Xiong Y H, Ning Y Q, & Fu M W, *J Alloys Compd*, 803 (2019) 16.

10   Wang J J, Guo W G, Li J H, & Zhou P, Mater High Temp, 34 (2017) 157.

11   Yuan K B, Guo W G, Li P H, Zhang Y, Li X L, & Lin X, *Mech Mater*, 135 (2019) 13.

12   Wang L, Yao C L, Shen J, Zhang Y P, Wang T, Xu H X, & Gao L H, *Master Sci Eng A*, 744 (2019) 59.

13   Wang L, Shen J, Shang Z, & Fu H Z, *Scr Mater*, 89 (2014) 1.

14   Wang L, Shen J, Zhang Y P, Fu H Z, *Mater Sci Eng A*, 664 (2016) 188.

15   Wang L, Shen J, Zhang Y P, Guo L L, Xu H X, Fu H Z, *Intermetallics*, 84 (2017) 11.

16   Mei R B, Li B, Fei H, Zhang X, Qi X W, & Liu X H, *Mech Mater*, 125(2018) 110.

17   le Graverend J B, Cormier J, Gallerneau F, Villechaise P, Kruch S, & Mendez J, *Int J Plast*, 59 (2014) 55.

18   Kotkunde N, Deole A D, Gupta A K, & Singh S K, *Mater Des*, 55 (2014) 999.

19   Guo J H, Zhao S D, & Yan G H, Mater *Sci Tech*, 29 (2013b) 197.

20   20Lin Y C, Li L T, & Fu Y X, *J Mater Sci*, 47 (2012) 1306.

21   Zhang P, Hu C, Zhu Q, Ding C G, & Qin H Y, *Mater Des*, 65 (2015) 1153.

22   Zhao J, Ding H, Zhao W, Huang M, Wei D, & Jiang Z, *Comput Mater Sci*, 92 (2014) 47.

23   Xu K, Liu G Q, Hu B F, Wang C Y, & Zhang Y W, *Master Sci Eng A*, 58 (2011) 4620.

24   Wu K, Liu G, Hu B, Li F, Zhang Y, Tao Y, & Liu J, Mater Des, 32(4) (2011) 1872.

25   Shamsolhodaei A, Zarei-Hanzaki A, Ghambari M, & Moemeni S, *Intermetallics*, 53 (2014) 140.